Hierarchical Porous Structure Fabrication Via Hybrid Stereolithography and Inkjet Printing With Sacrificial Liquid

Yeowon Yoon
Center for Advanced Manufacturing;
Department of Aerospace and Mechanical Engineering,
University of Southern California,
Los Angeles, CA 90007
e-mail: yeowonyo@usc.edu

Yang Xu
Center for Advanced Manufacturing;
Daniel J. Epstein Department of Industrial and Systems Engineering,
University of Southern California,
Los Angeles, CA 90007
e-mail: yxu195@usc.edu

Yong Chen[1]
Center for Advanced Manufacturing;
Department of Aerospace and Mechanical Engineering;
Daniel J. Epstein Department of Industrial and Systems Engineering,
University of Southern California,
Los Angeles, CA 90007
e-mail: yongchen@usc.edu

Inspired by porous morphology in nature, such as bone and lung tissues, synthetic porous materials are widely adopted in engineering applications that require lightweight, thermal resistance, energy absorption, and structural flexibility. One of the main challenges in the current porous material manufacturing techniques is their limited control over individual pore size, connectivity, and distribution. This paper presents a novel additive manufacturing process to fabricate porosity-embedded structures by integrating stereolithography and inkjet printing using a sacrificial liquid–water. A solenoid-based inkjet nozzle dispenses water droplets onto a layer of liquid photopolymer resin. Then the resin layer is photocured by a mask image projection device using a digital light processing device. The photocuring process defines the layer profile and captures the deposited water droplets in the solidified layer. The refilled fresh resin will further embed water droplets and form a new layer for the subsequent water droplet deposition. Three-dimensional (3D) structures with embedded water droplets can be printed layer-by-layer. The captured water will evaporate when heated, leaving an air-filled porous 3D structure. By selectively depositing water droplets and varying inkjet printing parameters, including pressure, nozzle opening time, and jetting frequency, the micropores whose sizes from 100 μm to 500 μm and distributions within the 3D-printed part can be modulated. This hybrid process can fabricate 3D structures with homogenously distributed pores and graded polymer structures with varying porosities. The elastic modulus of 3D-printed foam structures in different pore distributions has been tested and compared. [DOI: 10.1115/1.4055893]

Keywords: porous materials, additive manufacturing, functionally graded materials, stereolithography, inkjet printing, rapid prototyping and solid freeform fabrication

1 Introduction

Porosity-embedded materials can be discovered both in natural and artificial materials. In nature, porous medium exists on multiple scales, including alveolar tissues in lungs, bone, marine sponges, and honeycomb shapes in beehives (Fig. 1(*a*)). Nature's adoption of such porous structures comes for various reasons. For example, pore structures in the lung increase the surface area to exchange gas more efficiently. Also, pores in the skull bone contribute to reduced weight and energy impact to protect the brain. Hexagonal pore shapes in beehives are designed to minimize the consumption of building materials and to withstand the most weight. Inspired by the advantages of such natural porous media, synthetic porous materials have been designed to adopt the benefits of lightweight, low thermal conductivity, high surface region, high energy damping, and structural flexibility. Porosity-embedded synthetic materials with these advantages were demonstrated in many applications such as scaffolds for tissue engineering [5,6], selective liquid absorbers [7], energy harvesting devices [8,9], energy absorbers [10], pressure sensors [11], and acoustic materials [12].

A common fabrication strategy to generate porosity in synthetic materials is to use a template to create voids inside the deposited materials where the initial templates are removed after material deposition. For example, a commonly used fabrication method, replica molding [13–15], uses an existing porous template, which can be natural or synthetic, to be filled with base materials, followed by removing the template to create voids. While this method can use a wide variety of preexisting porous templates, the freedom of structural fabrication is limited to the structures that can be obtained from an original structure. Another method to create porosity is to use sacrificial templates [16,17]. The sacrificial templating uses micro/nanoscale droplets or particles to be mixed with base materials; hence the temporary template can create selective voids inside the materials. In sacrificial templating, control of pores size and concentration is now possible with maneuverability in sacrificial materials. However, removing the sacrificial material can still restrict the applications to limited material pools and structures. In comparison, the direct templating method can resolve this issue by adopting a gas medium as sacrificial layers [18–20]. When using direct templating, foaming agents can help create gas foams inside materials that allow a high porosity.

To further increase freedom in structural shapes and material pools, additive manufacturing (AM) has enabled the direct fabrication of controlled porosity inside base materials. For example, direct ink writing on a microscale was used to fabricate strut-based features [21]. Stereolithography based on photosensitive polymers was also used to directly print microscale strut structures [22] and template materials for creating structures with porosity [23,24]. To further scale down the manufacturing resolution, a nanoscale porous lattice structure was demonstrated using the two-photon polymerization process [25]. Microfluidic printing systems and functional drop-on-demand printing were also shown to create functionally graded materials with hollow structures [26,27]. Directly writing gas-inclusive bubbles to form porous polymers has recently demonstrated the capability of fabricating 3D structures with programable pores [28,29]. Still, the individual control of single pore size, distribution, and connectivity remains a core challenge for AM in fabricating porous materials with desired properties.

[1]Corresponding author.
Manuscript received July 3, 2022; final manuscript received October 1, 2022; published online December 1, 2022. Assoc. Editor: Sam Anand.

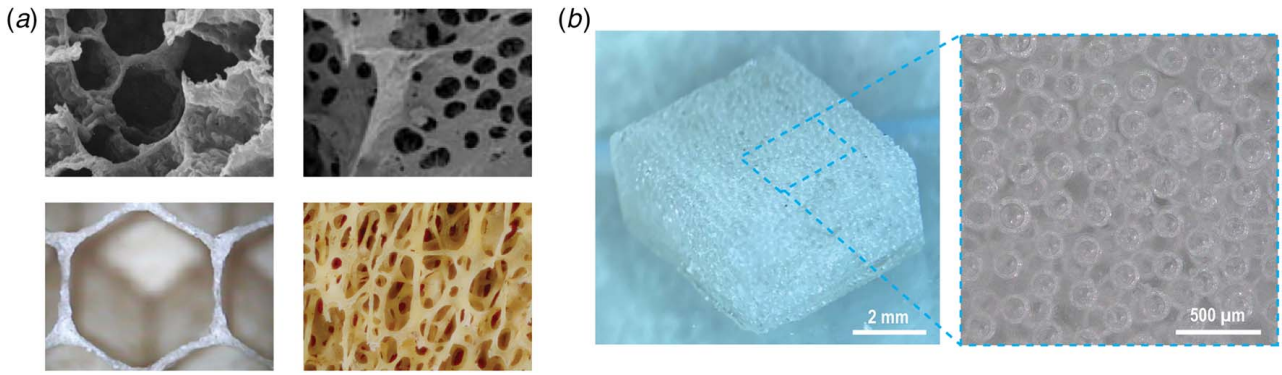

Fig. 1 Image of porous structures: (*a*) porosity-embedded structures in nature (alveolar tissue [1] (Reprinted with permission from Elsevier © 2010) sea sponge [2] (Creative Commons Attribution CC BY 4.0), cancellous bone [3] (Creative Commons Attribution CC BY 4.0), and honeycomb structure in the beehive [4] (Reprinted with permission from Royal Society © 2010), (from left top to clockwise), and (*b*) a 3D-printed porous cube

In this work, we present a novel AM method using stereolithography and inkjet printing of sacrificial liquids to create porosity-embedded polymer structures (Fig. 1(*b*)). A solenoid inkjet nozzle dispenses water droplets in a layer of liquid photopolymer resin; then the UV photocuring process defines planar layer shapes that capture the embedded water droplets in the layer. The process is repeated by introducing another layer of liquid resin and water droplets. After the layer-by-layer printing process finishes, the captured water droplets will go through a drying process to create a porous structure with air. This hybrid AM approach enables selective control of pore size and concentration in a 3D structure by adjusting inkjet printing parameters so the size and density of liquid droplets in each layer can be controlled.

2 Principle

The main idea of the hybrid AM process is to combine the top-down free-surface-based stereolithography [30,31] with the selective inkjet dispensing of water droplets. Here the stereolithography process defines polymer layer in high accuracy and resolution and the dispended water droplets are used as sacrificial materials inside the photocured polymer to create voids. Since most photocurable resins are hydrophobic, a water droplet will maintain its shape after jetting it into liquid resins. The concept of using liquid droplets to create porous morphology on polymer surfaces has been demonstrated in the templating methods where condensed liquid droplets form a monolayer of porous layer on liquid polymer films or where the liquid is directly mixed with polymer as emulsion [24,32,33].

Contrary to condensation or emulsion where droplet locations are randomly decided, direct dispensing of liquid droplets by inkjet nozzles is adopted in this work to selectively place water droplets inside a solid object. Figure 2 shows the fabrication steps of the hybrid AM process. First, a jet stream of liquid droplets generated by a solenoid valve is placed on the top layer of liquid resin while the printing head is moving along the *XY* plane (Fig. 2(*a*)). When the sacrificial liquid, double-distilled (DI) water used in the study, is dispensed onto the liquid resin surface, the dispensed liquid forms a spherical shape on the resin surface due to internal molecular bonding and the tendency of water being immiscible with liquid resin. Since the density of water (1.0 g/cm^3) is lighter than that of liquid resin (1.18 g/cm^3), the water droplet floats near the resin surface with the top portion of the droplet open to the air. A UV light pattern defined by a digital light processing (DLP) module then cures the photocurable resin (Fig. 2(*b*)). The cured polymer layer then secures the liquid droplets inside the polymer at their deposited positions. Before the photocuring step, the location of the dispensed water droplets inside liquid resin is affected by both surface flow and attractive capillary force. The printhead is retreated to avoid interference with the projection pattern during this step. After photocuring, the build plate moves down to completely dip the cured layer inside the liquid resin and then rises to form the single-layer thickness for the next layer of printing. A blade mounted on a linear stage scrapes the surface to flatten the liquid resin surface (Fig. 2(*c*)). After repeating these steps in multiple layers (Figs. 2(*d*) and 2(*e*)), the 3D-printed object is separated from the build plate. Finally, the cleaned object is placed on a heating plate (at 60 °C) to remove water captured inside the pores (Fig. 2(*f*)(i), (ii)).

3 Experiments

3.1 Experimental Setup. The experimental setup for the hybrid AM method is constructed by modifying a commercial fused deposition modeling (FDM) printer (Ender 5, Creality) into a customized hybrid prototype (Fig. 3(*a*)). While the three-axis

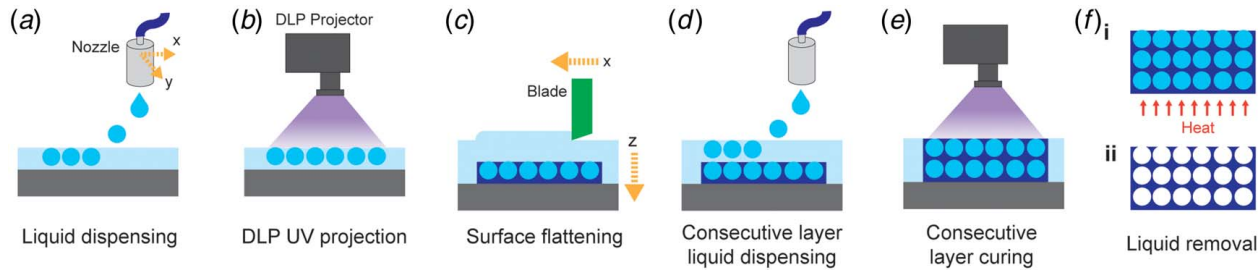

Fig. 2 Schematic illustration of the fabrication steps of the hybrid printing process: (*a*) liquid droplet dispensing, (*b*) UV curing with DLP area projection, (c) surface flattening with liner blade, (*d*), (e) dispensing sequential layers of liquid dispensing and UV curing, and (*f*) sample separation from (i) build plate and heating process and (ii) the fabricated porous structure after liquid removal

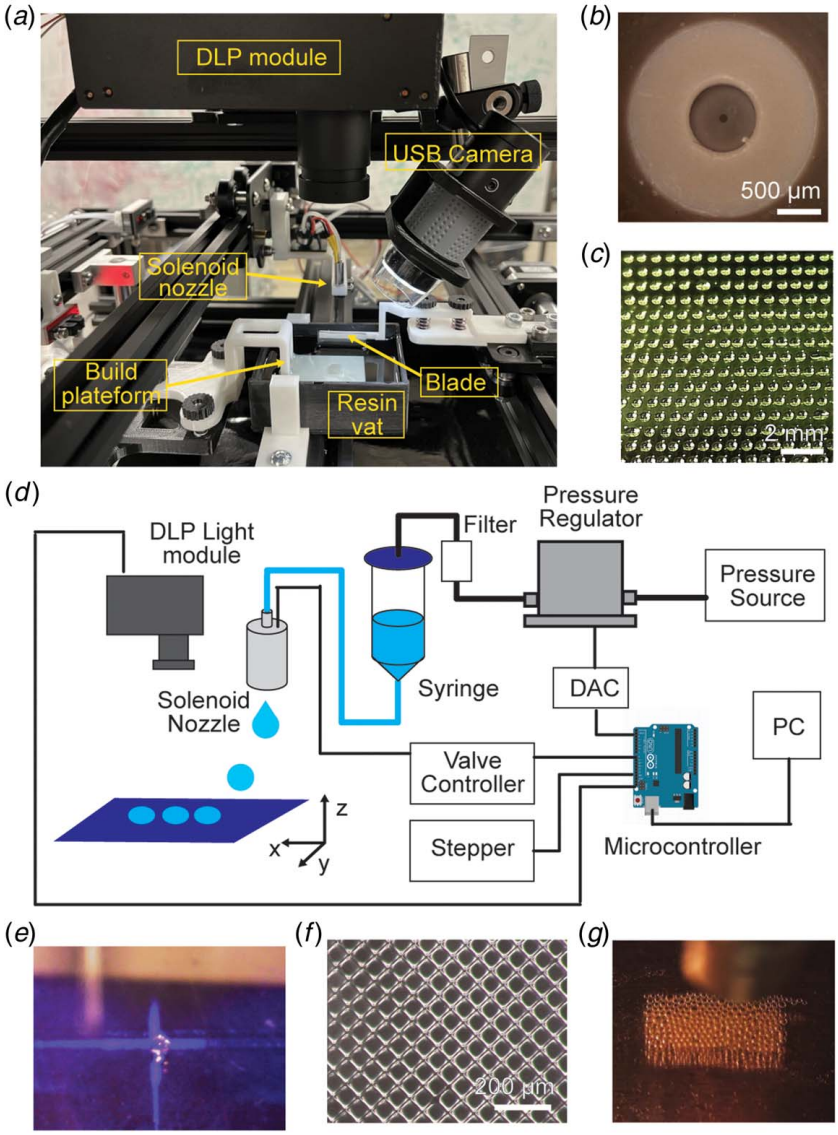

Fig. 3 Details of the experimental setup: (*a*) image of the experimental setup, (*b*) image of the solenoid nozzle valve, (*c*) deposited water droplets on a glass surface, (*d*) schematic illustration of the setup system, (*e*) alignment process with the DLP optics and the printing nozzle, (*f*) microscopic image of a cured surface, and (*g*) image of the liquid dispensing process on the resin surface

motion system was maintained, the FDM printhead was replaced by a solenoid valve (INKA2455010H, Lee Engineering). The inner diameter of the nozzle is 130 μm. The housing of the nozzle can hold 30 μL internal volume and endure up to 30 psi (Fig. 3(*b*)). The nozzle can handle up to 1 kHz of operation frequency while maintaining a printing distance of 10 mm between the nozzle end and the target surface. The performance of the solenoid nozzle was tested by printing water droplets onto the glass substrate (Fig. 3(*c*)). A DLP projector module (SprintRay, Los Angeles, CA) is installed on the build plate, where the distance between the build plate and the projector lens is maintained at 75 mm. A build platform is assembled on the *Z*-axis with three installed knobs to adjust the flatness of the resin surface. A blade mounted with a linear stage is used to recoat the liquid resin with a set layer thickness.

The jetting liquid is supplied to the solenoid valve through a syringe reservoir, where pressure is applied by an electrical pressure regulator (ITV0030-2UBL, SMC). The releasing and closing time of the valve is controlled by a pulse width modulation signal created by a microcontroller (Arduino Mega). The pressure level, the blade movement by a stepper motor, and the projection pattern of the DLP module (ON-OFF control of pixels) are all controlled by the microcontroller and a personal computer (Fig. 3(*d*)). To simultaneously dispense the liquid streams and cure them with the DLP system, the nozzle position and the DLP projection pattern must be aligned. It is assumed that, since the DLP module's projection area is fixed to the printing frame, the printing accuracy is mainly determined by the movement of the inkjet nozzle. Before printing, calibration was performed to minimize the positioning error from the inkjet nozzle. The calibration of the two systems was done by projecting an alignment pattern on the printing surface and then adjusting the nozzle position to the alignment pattern (Fig. 3(*e*)). The nozzle positions were then recorded at five different positions of a designed alignment pattern to synchronize the nozzle moving plane with the projection area. The pixel resolution of the DLP module is 1280×1024, and the pixel size is 62 μm. The single-pixel size is represented at the printing surface, where grid lines defined by the digital mirror device are clearly visible (Fig. 3(*f*)). Finally, a universal serial bus camera is installed to monitor the printing operation in vivo (Fig. 3(*g*)). This work

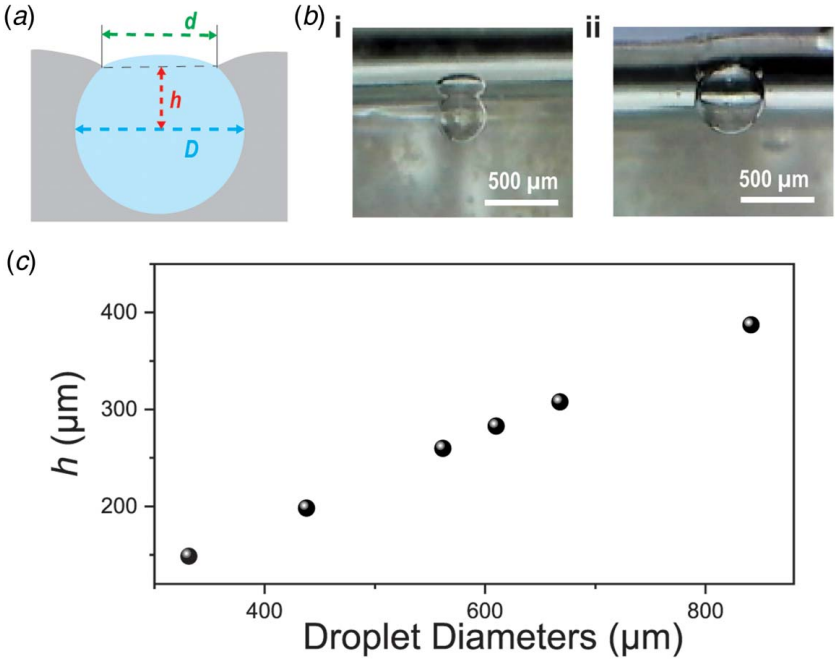

Fig. 4 Sacrificial liquid and resin interface: (*a*) schematic illustration of a water droplet at the resin surface, (*b*) an microscopic image of water droplets on the resin surface whose diameters are (i) 350 μm, (ii) 480 μm, respectively, and (c) calculated droplet vertical position in a function of droplet diameter

selected a clear soft resin (UV DLP Flexible Resin, PhotoCentric) as the photopolymer resin for its desirable mechanical properties.

Unlike typical inkjet printing where a droplet is jetted onto a solid substrate surface, the liquid droplets in the hybrid AM process are jetted onto a liquid resin surface. Therefore, the position of a droplet on the *Z*-axis can be affected by both the buoyancy of the liquid droplet and the flow of resin fluid. Under the condition that the resin layer thickness is larger than the droplet diameter, the vertical position of the water droplet is determined by the density, volume, and interfacial tension of the sacrificial liquid and the photocurable resin [34,35]. The vertical position of the droplets is described as the distance between the center of the droplet and the resin surface (h) in Fig. 4(*a*), where h is calculated by measuring both opening diameter (d) and droplet diameter (D). From the measurements of the opening and droplet diameters result using microscopic inspection, the calculated distance from the surface is plotted with the droplet's size, where the vertical center position of the droplet increases with droplet size (Figs. 4(*b*) and 4(*c*)). Since the vertical location of a droplet is set by its droplet size, additional depth alignment is not required in the printing process.

3.2 Manufacturing Process and Parameters. The process flowchart of the fabrication process is shown in Fig. 5. The initial step is to load planned mask images and nozzle toolpath defined in sequence (G-code) into the controller software. Accordingly, the machine prepares for the printing job by initializing all the *X*, *Y*, and *Z* stepper motors and then curing the first resin layer. After finishing the printing of the layer, the build plate is submerged into the resin vat. Like the laser-based stereolithography apparatus (SLA), a linear blade movement is used to flatten the resin surface and recoat a thin layer of liquid resin, in which the nozzle will dispense liquid droplets. Afterward, the layer is cured with the planned mask images in sequence. The layer-based building process is repeated until the final layer is finished.

A key manufacturing parameter in the hybrid AM process is to understand the solenoid nozzle's working range in controlling water droplets' sizes and positions. The generation of the jetting stream is affected by a set of printing parameters, including nozzle releasing time (valve opening time), nozzle holding time (valve closing time), dispensing frequency, driving amplitude of valve, pressure, and fluidic properties of dispensing materials. Among these parameters, the solenoid operation frequency, f, can be calculated as

$$\text{Jetting frequency, } f = 1/(t_r + t_h) \tag{1}$$

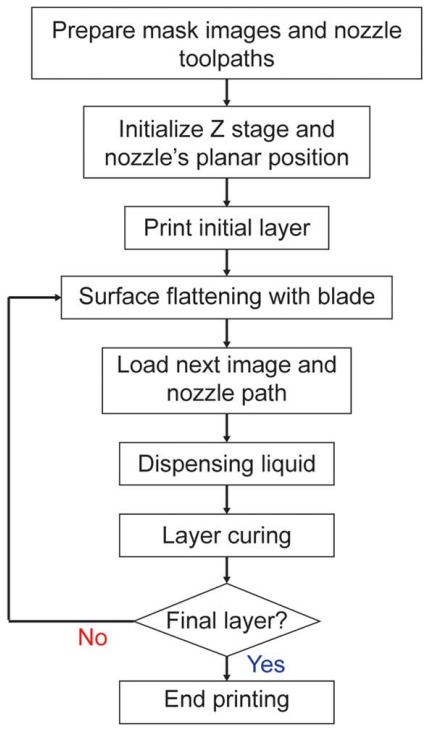

Fig. 5 Manufacturing process flowchart of the hybrid AM system based on stereolithography and inkjet printing

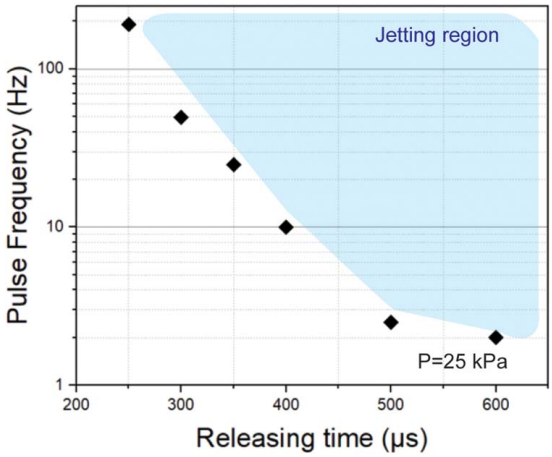

Fig. 6 Successful jetting printing conditions under different pulse frequencies and releasing times at the pressure level of 25 kPa

Where t_r is the releasing time and t_h is the holding time. If the nozzle frequency is higher, the nozzle will dispense liquid droplets faster. If t_r is smaller, the nozzle will allow a smaller amount of liquid to be dispensed since the nozzle's opening time is shorter.

In this study, the solenoid nozzle was tested by reducing the releasing time at a constant pressure to find where the smallest droplets of jetting stream region can be achieved. In Fig. 6, the successful jetting formation conditions of the pulse frequency upon a different releasing time were measured. At 400 μs release time, the operation frequency below 10 Hz cannot generate jetting stream; in comparison, the nozzle can create droplets with a frequency higher than 10 Hz. To its limit, if the release time is 250 μs, jetting streams can only be formed at a pulse frequency above 190 Hz. If the frequency is lower than this level, the valve generates no liquid droplets. Hence, a shorter release time of the nozzle requires a higher pulse frequency, indicating that a higher frequency helps to form a stable jetting stream. While the jetting conditions will change for different dispensing materials and nozzle sizes, similar experiments can be performed to ensure suitable jetting parameters are selected from the valid jetting region (Fig. 6—highlighted area in shading).

3.3 Liquid Removal Process. A core idea of the hybrid AM process is to create voids inside 3D-printed polymer layers by removing the original template of liquid bubbles. In this work, DI water was chosen as a sacrificial liquid. Test samples where liquid droplets were captured inside the photocured polymer were fabricated to test how well the liquid bubbles evaporate from the fabricated polymer structures (Fig. 7(*a*)). First, microscopic images of the test samples with printed water bubbles (diameter of 280 μm) were compared before and after 3 h of heating at 60 °C (Fig. 7(*b*)). From the microscopic view, the embedded pores after the heating look clearer than without the heating process where the embedded pores were filled with water. The microscopic view indicates that after the heating process, the pores do not contain a liquid medium.

To further observe this evaporation process, test samples (size of 6 mm × 6 mm × 3 mm, bubble diameter of 250 μm) were prepared where multiple layers of water bubbles were encapsulated inside the photocured polymer. The water bubbles were enclosed by solid polymer walls with varying distances to the part boundary. The samples were then placed on the heating plate while monitoring the weight loss. The initial weight of one sample (140 mg) was reduced to 119 mg after 8 h of the drying process (Fig. 7(*c*)). This 15% of weight loss in the sample indicates that the embedded water bubbles are gradually escaping from the surrounding

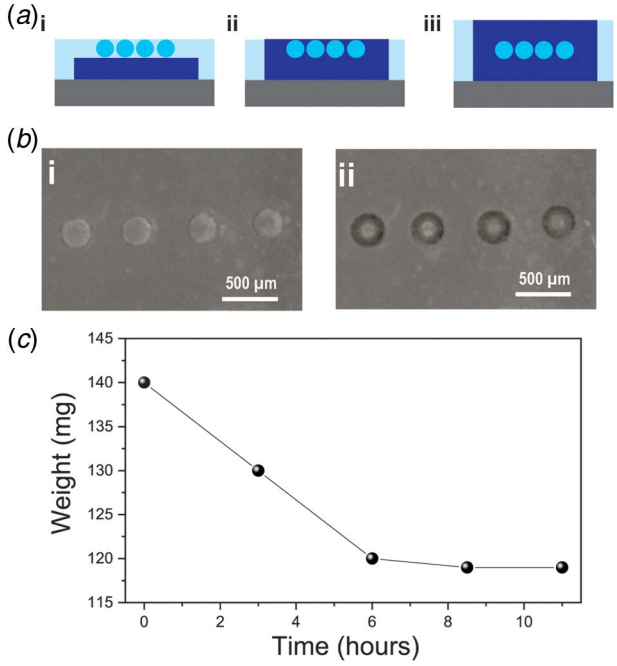

Fig. 7 Liquid removal process: (*a*) schematic illustration of the fabrication steps of test samples ((i) liquid bubble dispensing, (ii) curing of captured bubbles, and (iii) final curing of solid top layer), (*b*) top microscopic view of embedded bubbles filled with (i) water and (ii) after the drying process, and (c) measured total weight of a test sample overheating time

polymer structure during the drying process at 60 °C. As the water molecules leave the polymer network, air replaces the hollow pores. Furthermore, we compared the droplet sizes before and after the drying process. We found the measured diameter change was less than 1%, indicating no significant shape distortion in the liquid removal process. We assume, by raising the polymer's temperature, its network expands so water molecules will evaporate and escape from the polymer enclosure in a dry environment. The drying process will take longer for a droplet with a larger distance to the part boundary.

4 Planar Printing

4.1 Single Droplet Size Control. The size of the deposited water droplets in liquid resin has been studied using various nozzle printing parameters. The controlled parameters are nozzle release time, operation frequency, and applied pressure. The diameters of the printed droplets were compared using different printing conditions. For example, when the nozzle release time is set at 500 μs, the sizes of single droplets are compared by applying various pressures to the nozzle (Fig. 8(*a*)). Given that the maximum operating pressure of the selected nozzle is 200 kPa, the applied pressure was set at 20, 50, 100, and 150 kPa for the experiments. The droplet diameters increase with the applied pressure where the nozzle frequency is set at 97 Hz. Under different printing parameters, droplet sizes vary from 107 μm to 515 μm. A longer release time increases droplet size (Fig. 8(*b*)). When the release time is fixed at 300 μs, a higher nozzle frequency results in a larger droplet size (Fig. 8(*c*)). In most cases, the droplet size differences are most evident in the range of 20–50 kPa.

4.2 Line Printing. After characterizing the printing parameters for a single droplet, the linear printing of a line of water droplets was performed to understand the critical pitch distance between water droplets in liquid resin. In one-dimensional line printing,

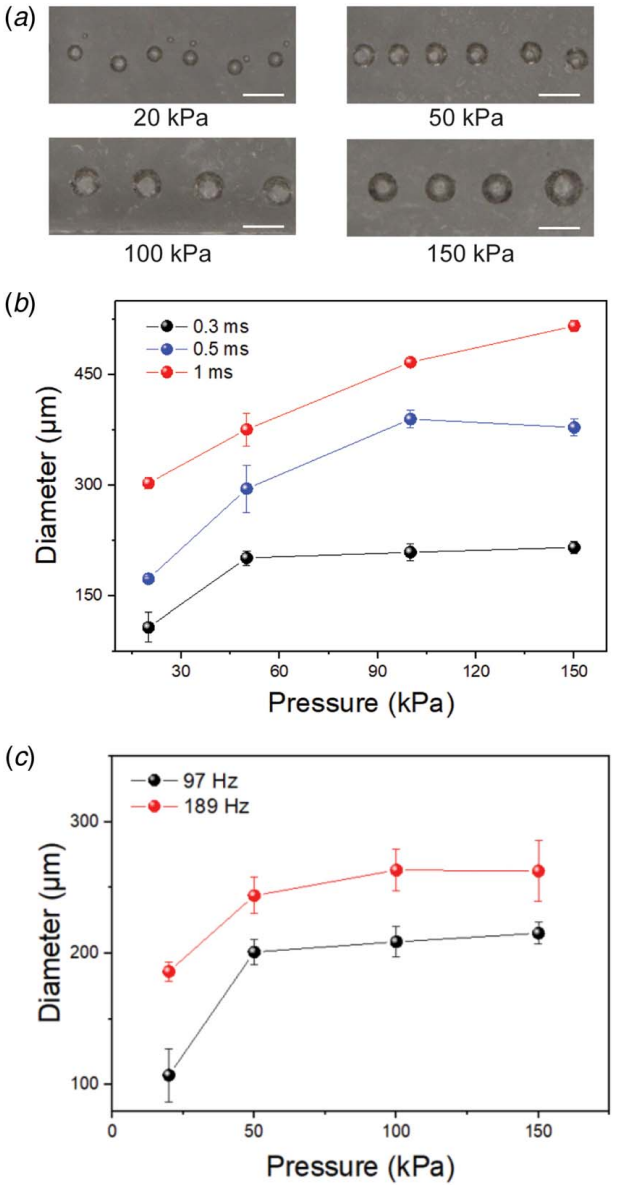

Fig. 8 Single droplet size characterization: (*a*) image of the printed pores in various pressure ranges, (*b*) measured droplet diameters over different pressures and release times, and (*c*) measured droplet diameters over different pressures and jetting frequencies. All scale bars are 500 μm.

the distance between droplets is determined by the nozzle's translation speed. The pitch distance, p_x can be calculated from

$$\text{Pitch,} \quad p_x = v/f \tag{2}$$

where v is the nozzle's planar moving speed, and f is the jetting frequency. From Eq. (2), the pitch size is proportional to the planar moving speed of the nozzle. By applying different moving speeds from 35 mm/s to 10 mm/s, where nozzle release time was set at 300 μs, with a frequency of 97 Hz and a pressure of 10 kPa, the droplets were designed to have a pitch distance from 103 μm to 360 μm, respectively (Fig. 9(*a*)). The diameter of a single droplet is 160 μm and 256 μm when the pressure is set at 10 kPa and 20 kPa, respectively.

The measured pitch distance between two droplets increases after the calculated pitch distance gets smaller than the size of the droplets (Fig. 9(*b*)). If two adjacent droplets do not merge into a single droplet, the measured pitch distance follows the reference dash line. However, in both 10 kPa and 20 kPa, when the pitch size gets smaller than the droplet diameter, the measured pitch distance between two adjacent droplets starts to increase, indicating two adjacent droplets begin to merge into a single droplet, which leads to a larger droplet size. As shown in Fig. 9(*c*), the droplet sizes were measured with the pitch size decreasing from 350 μm to 100 μm. In both cases of 10 kPa and 20 kPa, once the pitch distance (in the *X*-axis) gets smaller than the diameters of single droplets (160 μm and 256 μm, respectively), the size of the single droplet increases. Hence, the line printing pitch distance needs to stay larger than the diameter of a single droplet during printing to avoid adjacent droplets merging.

4.3 Planar Density Control. To increase the printing dimension in two dimensions, pitch distances (both p_x and p_y as shown in Fig. 10(*a*)) are considered. Similar to line printing, multiple lines are drawn for a planar layer with controlled density. Still, p_x is controlled by setting different nozzle speeds; however, p_y is simply line distance between two printing line paths. The unit square grid (marked in a dashed line) is the minimum rectangular grid unit whose length is pitch distances in the *X* and *Y* axes. To quantify how dense the jetted droplets are formed in the 3D-printed structure, the planar porosity value is calculated as

$$\text{Planar porosity} = \frac{\text{Area of droplet inside the unit grid}}{\text{Area of unit grid}} = \frac{\pi d^2/4}{p_x p_y} \tag{3}$$

where d is the droplet diameter. If there are no pores in the material, the porosity becomes zero indicating a solid layer. As the porosity increases, the density decreases. Theoretically, the maximum value of the planar porosity can be obtained at 0.907 where liquid droplets are forming honeycomb grids. As the size of the droplet increases with increasing pressure, the porosity of the planar pattern also increases (Fig. 10(*b*)).

5 3D Printing of Porosity-Embedded Structures

5.1 Printing Monodispersed Materials. After the printing parameters have been characterized in the planar dimensions, the next step is to test the printing process of 3D structures. As shown in Fig. 9(*c*), to print samples with individual pores sizes at 200 μm, the grid pitch distance is set at 250 μm to avoid the merging of adjacent droplets. For 300 μm-size pore sample, the grid pitch is set at 400 μm. In addition, to fabricate a porosity-embedded structure, the *Z*-layer thickness needs to be controlled according to the droplet size. For example, the layer thicknesses in both cases are set at 200 μm and 300 μm, respectively, to ensure printing uniformity in the *Z* direction. A cuboid structure having a dimension of 6.3 mm × 6.3 mm × 3 mm was printed through the hybrid AM process (Fig. 11). After the drying process to remove liquids, the density of 200 μm and 300 μm samples was measured at 0.903 g/cm^3 and 0.851 g/cm^3, respectively, whereas the density of a solid resin sample without any porosity is 1.18 g/cm^3. The density changes show that embedding porous regions in the solid material can lead to over 28% of density change in the 3D-printed structures. Further measurements show the printed cuboid sample's dimensions have *X-Y* dimensional error of 1.89% and a *Z* dimensional error of 1.70% in comparison with the solid printing sample without porosity.

The printing conditions for these test samples were designed to produce monodispersed materials. That is, the size of the pores is uniform under the same inkjet printing condition. Accordingly, the porosity (ϕ) of the printed structure with uniform pore sizes in individual layers can be estimated as

$$\text{Porosity,} \quad \varnothing = V_{\text{void}}/V_{\text{total}} \tag{4}$$

where V_{void} is the volume of the porous region, and V_{total} is the total volume of the printing part.

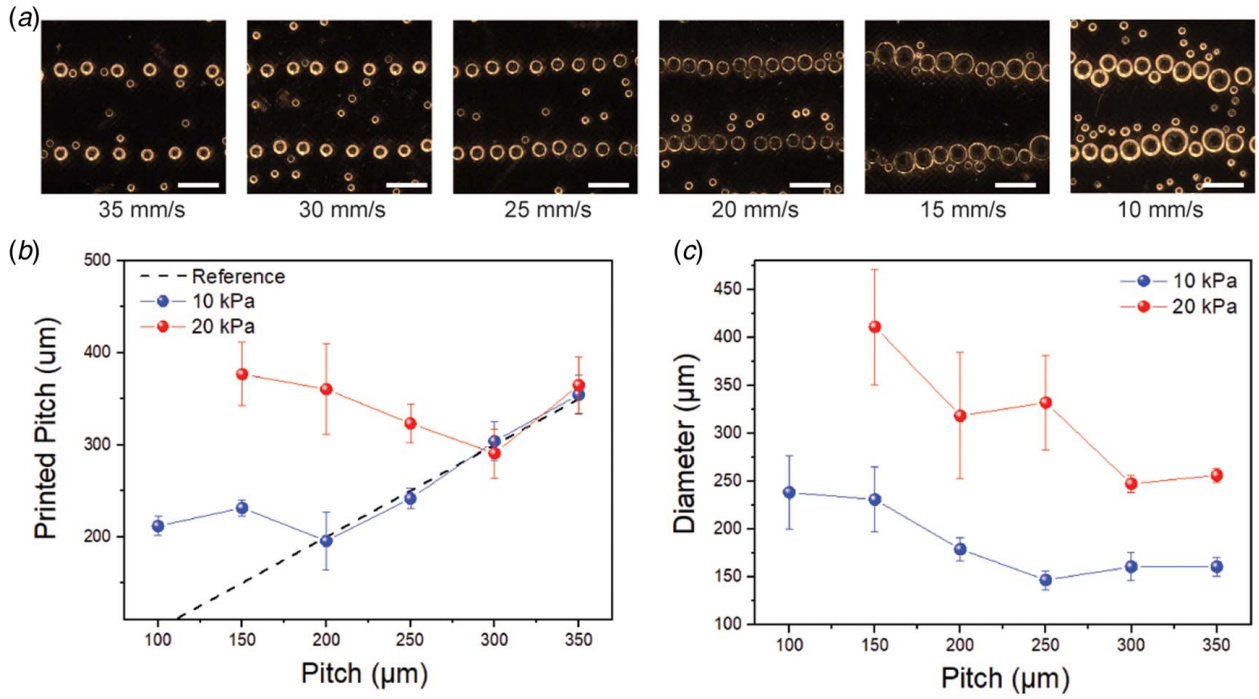

Fig. 9 Single line printing of droplets: (*a*) image of droplet printing results with the line nozzle moving at different speeds from 10 mm/s to 35 mm/s. Some small liquid satellites from nozzle printing are observed, (*b*) calculated pitch distance versus measured pitch distance, and (*c*) calculated pitch distance versus measured diameters of the printed droplets. All scale bars are 500 μm.

If we assume 3D printing of a cuboid structure with pores and the layer thickness stays larger than the pore diameter, the porosity is then calculated as

$$\varnothing_{\text{cuboid}} = \frac{(1/6)\pi n d^3}{wlh} \tag{5}$$

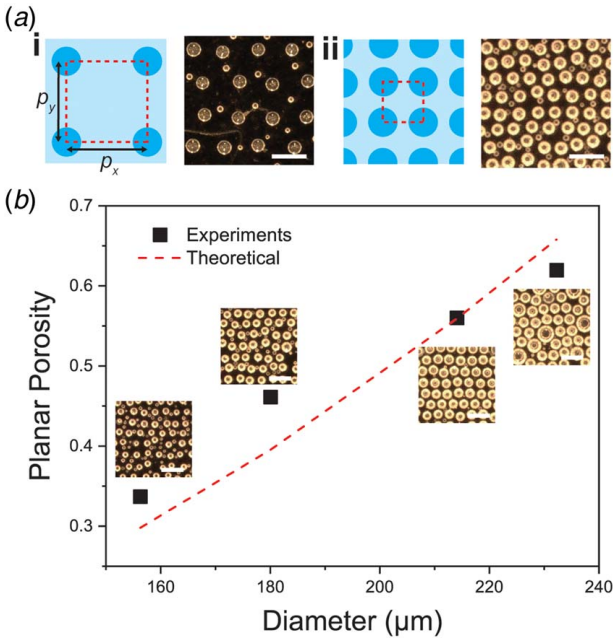

Fig. 10 Grid printing of droplets: (*a*) schematic of grid pitch and actual printing results where the pitch distance at (i) 500 μm and (ii) 250 μm and (*b*) droplet diameters versus planar porosity. All scale bars are 500 μm.

where n is the droplet number, d is the diameter of pores, w is width, l is the length, and h is the height of a single layer in the cuboid model, respectively. Using Eq. (5), the 200 μm-pore sample has porosity of 0.335, and the 300 μm-pore sample has porosity of 0.442.

A pyramid model with the size of 6 mm × 6 mm × 3 mm with the intended pore size of 200 μm was designed and then fabricated (Fig. 12(*a*)). Accordingly, the parameters set in printing the designed pyramid model are given in Table 1. A scaffold structure with the size of 6 mm × 6 mm × 2 mm having different strut widths (380 μm and 500 μm) was also designed and fabricated (Fig. 12(*b*)). The scaffold model has multiscale pores consisting of mesoscale rectangular voids and microscale spherical voids. The porosity of the scaffold can be calculated as

$$\varnothing_{\text{scaffold}} = \frac{\left(\frac{1}{6}\right)\pi n d^3 + a^2 m^2 h}{(ma + mt + t)^2 h} \tag{6}$$

where m is the number of voids per axis, a is rectangular void width, and t is strut width. For the strut size (t) of 380 μm, the calculated porosity is 0.727, which is 117% higher than the 3D-printed cuboid with only mesoscale voids constructed by DLP printing. The increased porosity suggests that, in addition to designing scaffold patterns for DLP-based 3D printing, it is possible to significantly increase structural porosity with embedded microscale pores that have a similar size to cells.

5.2 Graded Materials Printing. Since the size and distribution of the pores can be controlled by using different inkjet printing parameters, it is now possible to have different pore sizes and densities in the same 3D structure. If the pore size is fixed, pore density can be differentiated within the printed pattern by simply controlling pitch distance (i.e., nozzle moving speed) in the same printing path. In Fig. 13(*a*), the left region of the pattern was printed with a pitch size of 200 μm; the center region was printed with a 350 μm pitch size; and the right region was printed with a 500 μm pitch

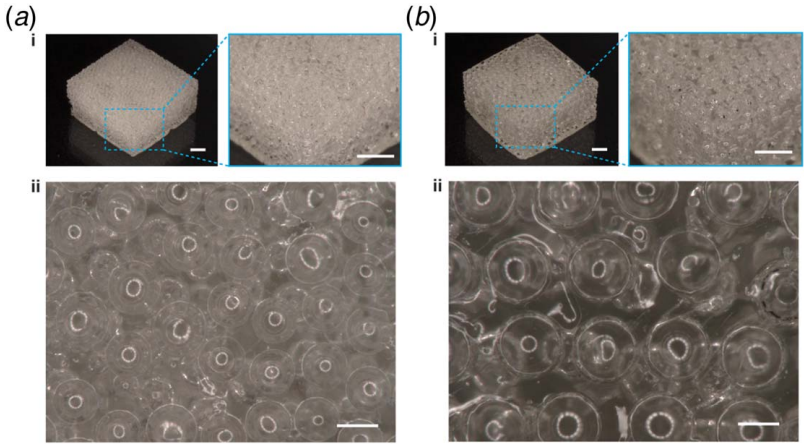

Fig. 11 3D-printed porous cuboid in different pore sizes: (*a*) the printing sample with individual pore size of 200 μm ((i) overall image of sample and (ii) microscopic image of top surface) and (*b*) 3D-printed sample with pore size of 300 μm. Scale bars are (i) 1 mm and (ii) 200 μm, respectively.

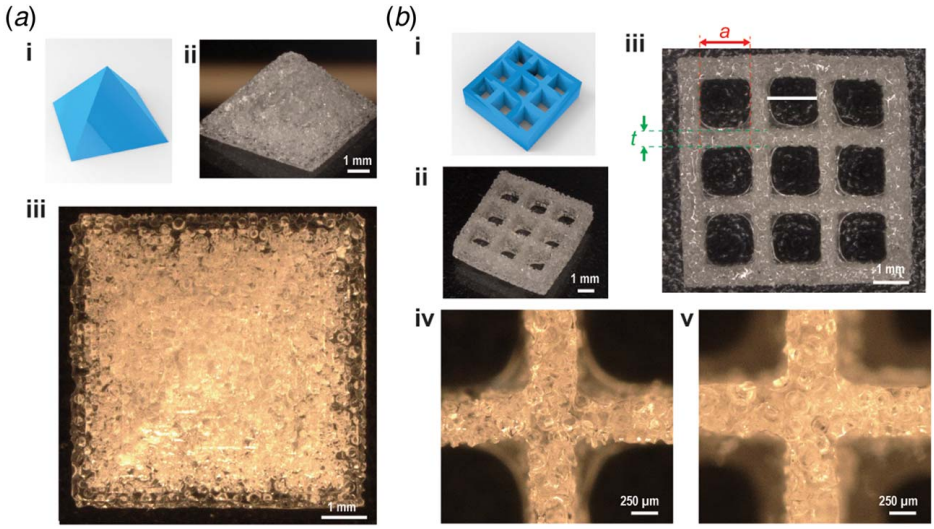

Fig. 12 3D printed porous structures in various shapes: (*a*) (i) CAD design of a pyramid and (ii) the 3D-printed pyramid with embedded porous layers, (iii) image from the top of the pyramid sample, (*b*) (i) CAD design of a scaffold and (ii), (iii) images of the 3D-printed scaffold with porous layers. Close-up image of scaffold surfaces in different strut (width) sizes of (iv) 380 μm and (v) 500 μm.

Table 1 Printing parameters of sample parts

Case	Pressure (kPa)	Release time t_r (μs)	Layer thickness (μm)	Pitch in X, p_x (μm)	Pitch in Y, p_y (μm)
Pyramid	50	300	200	250	250
Scaffold	30	300	200	250	250
Bottom layers	20	500	200	400	400
Mid layers	25	300	200	250	250
Top layers	10	300	100	170	200

size. Hence, in the same printing plane, the planar density varies from 0.21 to 0.12.

Furthermore, different pore sizes were printed in different layers to demonstrate the local density control with gradient variation (Fig. 13(*b*)), where the bottom layers are printed with relatively large pores (300 μm). The size of the pores gradually reduced to mid-size pores (200 μm) and eventually reached small-size pores (150 μm) in the top layer along the Z direction (Fig. 13(*c*)). The printing parameters for each layer with different pore sizes are shown in Table 1. The layer thickness along the Z-axis also changes according to the designed pore sizes. To closely examine the graded pore size changes, the 3D-printed cuboid sample was cut with a razor blade to examine its cross-sectional view (Fig. 13(*c*)).

During the multilayer 3D printing processes, if the diameter of the liquid droplet is larger than the layer thickness, the accumulated droplets in the vertical Z direction are connected through layers. For example, when the diameter of the droplets is 250 μm and the layer thickness is 200 μm, droplets positioned in identical planar positions but in different layers form a connected path where the pores in the neighboring layers are connected (Fig. 13(*d*)). Furthermore, these interconnected pores leave undulating wall geometry along the vertical direction, which will be investigated further in our future study.

6 Mechanical Property Testing

Mechanical compressive testing was performed on samples with different densities to study how different pore sizes and material densities can affect the mechanical property of 3D-printed porosity materials. A force gauge (M7-05, Mark-10) was used to measure force change while the flat-end gauge moved along the linear stage (velocity 0.1 mm/s). The 3D-printed cuboid samples were cut into the dimension of 3 mm × 3 mm × 3 mm for the compressive test.

Three types of samples were prepared for mechanical property measurement and comparison: solid, pore sizes of 180 μm (pore A, Fig. 14(*a*)(i)), and pore sizes of 280 μm (pore B, Fig. 14(*a*)(ii)). The densities of each sample are at 1.1, 0.81, and 0.67 g/cm^3, respectively. The stress-strain curve of the samples indicates that the solid sample without any porosity has the highest inclination while the low-density models show the lowest inclination (Fig. 14(*b*)). The elastic moduli of the tested samples are calculated at 2.29, 1.57, and 1.25 MPa, respectively (Fig. 14(*c*)). The modulus of the samples is proportional to the material density with the linear fitting slope of 2.4 MPa/(g/cm^3).

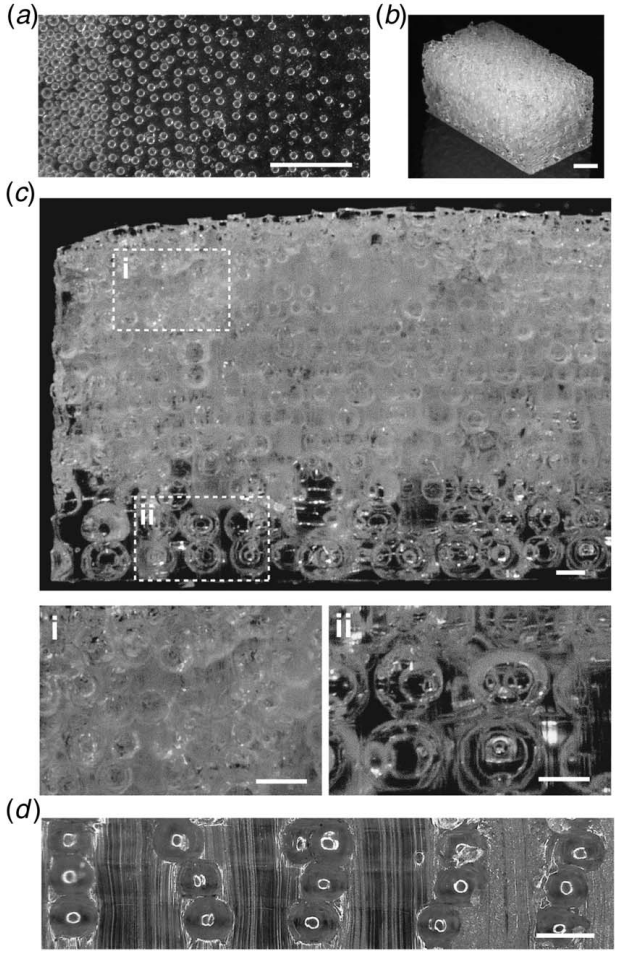

Fig. 13 Graded pore distributions, sizes, and connectivities in the vertical direction: (*a*) top view of a printing surface with different pore distributions, (*b*) 3D-printed cuboid with graded pore sizes, (*c*) cross-sectional views of (i) upper layers with small pores ($d = 150$ μm) embedded and (ii) lower layers with large pores ($d = 300$ μm) embedded, and (*d*) cross-sectional image view of connected pores in the vertical direction. Scale bars are (*a*), (*b*) 1 mm and (*c*), (*d*) 250 μm.

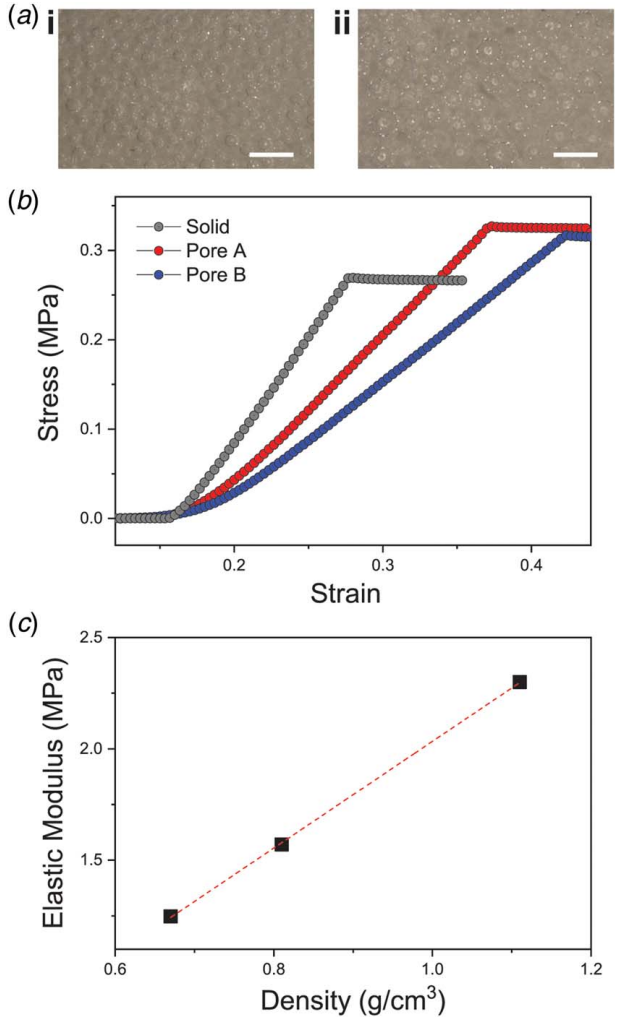

Fig. 14 Mechanical testing of printed samples: (*a*) image of (i) pore A sample and (ii) pore B sample, (*b*) stress curves in function of strain for different types of samples, and (*c*) summary of elastic modulus with different sample densities. All scale bars are 500 μm.

7 Conclusion

This paper presents a novel hybrid additive manufacturing method by integrating stereolithography and inkjet printing to fabricate porosity-embedded structures with controlled pore sizes and locations. The printing parameters, including pore size, line width, liquid removal, and density control, have been studied for the optimized hybrid printing process and desired porosity control. Various 3D-printed porous samples have been fabricated using the layer-by-layer approach, where pore sizes vary between 100 μm and 500 μm. Embedded micropores with different sizes in a single structure demonstrate the feasibility of achieving functionally graded materials using the hybrid AM process. The current fabrication approach can create porous materials with porosity up to

44.2% while modulating the material density up to 28%. The developed hybrid AM method enables control over individual pore size and density in a locally programable manner. Also, the mask projection-based building process can easily define the final shape of the 3D porous structure without relying on additional material processing steps.

While the proposed hybrid AM process enables 3D printing of porosity-embedded structures with pore size and distribution control, the hybrid process is slower than the projection-based stereolithography process [36,37] due to the use of the inkjet head to dispense liquids in each layer. Some other challenges of the process remain to be overcome as well. First, since the droplets from the inkjet nozzle are floating on the liquid surface, printing accuracy is affected by this free droplet movement in liquid resin. Hence printing quality of the inkjet nozzle is primarily affected by the interfacial forces between liquid droplets and resin flow since the liquid printing surface is not constrained. Second, liquid satellites from nozzle printing exist in the layer printing (refer to Fig. 9(*a*)). Increasing the line printing accuracy and reducing the printing defects due to liquid satellites need to be addressed to further increase the printing accuracy of the developed AM process. Finally, like other sacrificial material processes, a limited range of material selection pools for both structure and sacrificial materials have been tested in our work, where the structure material is a photosensitive polymer and the sacrificial material is DI water.

We envision this novel hybrid AM method can enable many new materials and applications. Some future works to be investigated include: (1) water as a highly removable sacrificial material can benefit the fabrication of parts with overhang features [38] and microfluidic channels [39], (2) a drop-on-demand approach can be introduced to create multi-functional composites with various ink droplets or particles as inclusions [26], (3) 3D printing of functionally graded material-based actuator and sensor applications, and (4) biomedical platforms based on porous structures can be used in tissue engineering including cell culturing in pore regions and bone structure regeneration [40].

Acknowledgment

The first author acknowledges the fellowship support from Viterbi School of Engineering at the University of Southern California (USC). We also thank Professor Hangbo Zhao at USC for his help in mechanical property testing.

Conflict of Interest

There are no conflicts of interest.

Data Availability Statement

The datasets generated and supporting the findings of this article are obtainable from the corresponding author upon reasonable request.

References

[1] Hsia, C. C.W., Hyde, D. M., Ochs, M, and Weibel, E. R., 2010, "How to Measure Lung Structure–What for? On the Standards for the Quantitative Assessment of Lung Structure" Respir. Physiol. Neuro., **171**(2), pp. 72–74.

[2] Leys, S. P., Yahel, G., Reidenbach, M. A., Tunnicliffe, V., Shavit, U., and Reiswig, H. M., 2011, "The Sponge Pump: The Role of Current Induced Flow in the Design of the Sponge Body Plan," PLoS One, **6**(12), p. e27787.

[3] Bishop, P. J., Hocknull, S. A., Clemente, C. J., Hutchinson, J. R., Farke, A. A., Beck, B. R., Barrett, R. S., and Lloyd, D. G., 2018, "Cancellous Bone and Theropod Dinosaur Locomotion. Part I—An Examination of Cancellous Bone Architecture in the Hindlimb Bones of Theropods," Peer J., **6**.

[4] Karihaloo, B. L., Zhang, K., and Wang, J., 2013, "Honeybee Combs: How the Circular Cells Transform Into Rounded Hexagons," J. R. Soc., Interface, **10**(86), p. 20130299.

[5] Wang, C.-C., Yang, K.-C., Lin, K.-H., Liu, H.-C., and Lin, F.-H., 2011, "A Highly Organized Three-Dimensional Alginate Scaffold for Cartilage Tissue Engineering Prepared by Microfluidic Technology," Biomaterials, **32**(29), pp. 7118–7126.

[6] Hutmacher, D. W., 2000, "Scaffolds in Tissue Engineering Bone and Cartilage," Biomaterials, **21**(24), pp. 2529–2543.

[7] Choi, S.-J., Kwon, T.-H., Im, H., Moon, D.-I., Baek, D. J., Seol, M.-L., Duarte, J. P., and Choi, Y.-K., 2011, "A Polydimethylsiloxane (PDMS) Sponge for the Selective Absorption of Oil From Water," ACS Appl. Mater. Interfaces, **3**(12), pp. 4552–4556.

[8] Cha, S., Kim, S. M., Kim, H., Ku, J., Sohn, J. I., Park, Y. J., Song, B. G., et al., 2011, "Porous PVDF as Effective Sonic Wave Driven Nanogenerators," Nano Lett., **11**(12), pp. 5142–5147.

[9] Mi, H.-Y., Jing, X., Zheng, Q., Fang, L., Huang, H.-X., Turng, L.-S., and Gong, S., 2018, "High-Performance Flexible Triboelectric Nanogenerator Based on Porous Aerogels and Electrospun Nanofibers for Energy Harvesting and Sensitive Self-Powered Sensing," Nano Energy, **48**, pp. 327–336.

[10] Li, M., Xu, L., and Lu, W., 2019, "Nanopore Size Effect on Critical Infiltration Depth of Liquid Nanofoam as a Reusable Energy Absorber," J. Appl. Phys., **125**(4), p. 044303.

[11] Yao, H., Ge, J., Wang, C., Wang, X., Hu, W., Zheng, Z., Ni, Y., and Yu, S., 2013, "A Flexible and Highly Pressure-Sensitive Graphene–Polyurethane Sponge Based on Fractured Microstructure Design," Adv. Mater., **25**(46), pp. 6692–6698.

[12] Del Rey, R., Alba, J., Arenas, J. P., and Sanchis, V. J., 2012, "An Empirical Modelling of Porous Sound Absorbing Materials Made of Recycled Foam," Appl. Acoust., **73**(6–7), pp. 604–609.

[13] Zampieri, A., Sieber, H., Selvam, T., Mabande, G. T., Schwieger, W., Scheffler, F., Scheffler, M., and Greil, P., 2005, "Biomorphic Cellular SiSiC/Zeolite Ceramic Composites: From Rattan Palm to Bioinspired Structured Monoliths for Catalysis and Sorption," Adv. Mater., **17**(3), pp. 344–349.

[14] Losic, D., Mitchell, J. G., Lal, R., and Voelcker, N. H., 2007, "Rapid Fabrication of Micro-and Nanoscale Patterns by Replica Molding From Diatom Biosilica," Adv. Funct. Mater., **17**(14), pp. 2439–2446.

[15] Han, J.-W., Kim, B., Li, J., and Meyyappan, M., 2013, "Flexible, Compressible, Hydrophobic, Floatable, and Conductive Carbon Nanotube-Polymer Sponge," Appl. Phys. Lett., **102**(5), p. 051903.

[16] Studart, A. R., Studer, J., Xu, L., Yoon, K., Shum, H. C., and Weitz, D. A., 2011, "Hierarchical Porous Materials Made by Drying Complex Suspensions," Langmuir, **27**(3), pp. 955–964.

[17] Chang, H.-K., Chang, G. T., Thokchom, A. K., Kim, T., and Park, J., 2018, "Ultra-Fast Responsive Colloidal–Polymer Composite-Based Volatile Organic Compounds (VOC) Sensor Using Nanoscale Easy Tear Process," Sci. Rep., **8**(1), pp. 1–11.

[18] Chen, Z., Xu, C., Ma, C., Ren, W., and Cheng, H., 2013, "Lightweight and Flexible Graphene Foam Composites for High-Performance Electromagnetic Interference Shielding," Adv. Mater., **25**(9), pp. 1296–1300.

[19] Vakifahmetoglu, C., Pippel, E., Woltersdorf, J., and Colombo, P., 2010, "Growth of One-Dimensional Nanostructures in Porous Polymer Derived Ceramics by Catalyst-Assisted Pyrolysis. Part I: Iron Catalyst," J. Am. Ceram. Soc., **93**(4), pp. 959–968.

[20] McCall, W. R., Kim, K., Heath, C., La Pierre, G., and Sirbuly, D. J., 2014, "Piezoelectric Nanoparticle–Polymer Composite Foams," ACS Appl. Mater. Interfaces, **6**(22), pp. 19504–19509.

[21] Lewis, J. A., 2006, "Direct Ink Writing of 3D Functional Materials," Adv. Funct. Mater., **16**(17), pp. 2193–2204.

[22] Zheng, X., Lee, H., Weisgraber, T. H., Shusteff, M., DeOtte, J., Duoss, E. B., Kuntz, J. D., et al., 2014, "Ultralight, Ultrastiff Mechanical Metamaterials," Science, **344**(6190), pp. 1373–1377.

[23] Song, X., Zhang, Z., Chen, Z., and Chen, Y., 2017, "Porous Structure Fabrication Using a Stereolithography-Based Sugar Foaming Method," ASME J. Manuf. Sci. Eng., **139**(3), p. 031015.

[24] Kleger, N., Minas, C., Bosshard, P., Mattich, I., Masania, K., and Studart, A. R., 2021, "Hierarchical Porous Materials Made by Stereolithographic Printing of Photocurable Emulsions," Sci. Rep., **11**(1), pp. 1–11.

[25] Meza, L. R., Das, S., and Greer, J. R., 2014, "Strong, Lightweight, and Recoverable Three-Dimensional Ceramic Nanolattices," Science, **345**(6202), pp. 1322–1326.

[26] Elsing, J., Quell, A., and Stubenrauch, C., 2017, "Toward Functionally Graded Polymer Foams Using Microfluidics," Adv. Eng. Mater., **19**(8), p. 1700195.

[27] Mea, H. J., Delgadillo, L., and Wan, J., 2020, "On-Demand Modulation of 3D-Printed Elastomers Using Programmable Droplet Inclusions," Proc. Natl. Acad. Sci. U. S. A., **117**(26), pp. 14790–14797.

[28] Visser, C. W., Amato, D. N., Mueller, J., and Lewis, J. A., 2019, "Architected Polymer Foams Via Direct Bubble Writing," Adv. Mater., **31**(46), p. 1904668.

[29] Amato, D. N., Amato, D. V., Sandoz, M., Weigand, J., Patton, D. L., and Visser, C. W., 2020, "Programmable Porous Polymers Via Direct Bubble Writing With Surfactant Free Inks," ACS Appl. Mater. Interfaces, **12**(37), pp. 42048–42055.

[30] Sun, C., Fang, N., Wu, D. M., and Zhang, X., 2005, "Projection Micro-Stereolithography Using Digital Micro-Mirror Dynamic Mask," Sens. Actuators, A, **121**(1), pp. 113–120.

[31] Xu, K., and Chen, Y., 2015, "Mask Image Planning for Deformation Control in Projection-Based Stereolithography Process," ASME J. Manuf. Sci. Eng., **137**(3), p. 031014.

[32] Wan, L.-S., Zhu, L.-W., Ou, Y., and Xu, Z.-K., 2014, "Multiple Interfaces in Self-Assembled Breath Figures," Chem. Commun., **50**(31), pp. 4024–4039.
[33] Connal, L. A., Vestberg, R., Gurr, P. A., Hawker, C. J., and Qiao, G. G., 2008, "Patterning on Nonplanar Substrates: Flexible Honeycomb Films From a Range of Self-Assembling Star Copolymers," Langmuir, **24**(2), pp. 556–562.
[34] Phan, C. M., Allen, B., Peters, L. B., Le, T. N., and Tade, M. O., 2012, "Can Water Float on Oil?," Langmuir, **28**(10), pp. 4609–4613.
[35] Wang, B., Wang, C., Yu, Y., and Chen, X., 2020, "Spreading and Penetration of a Micro-Sized Water Droplet Impacting Onto Oil Layers," Phys. Fluids, **32**(1), p. 012003.
[36] Pan, Y., Zhou, C., and Chen, Y., 2012, "A Fast Mask Projection Stereolithography Process for Fabricating Digital Models in Minutes," ASME J. Manuf. Sci. Eng., **134**(5), p. 051011.
[37] Li, X., Mao, H., Pan, Y., and Chen, Y., 2019, "Mask Video Projection Based Stereolithography With Continuous Resin Flow to Build Digital Models in Minutes," ASME J. Manuf. Sci. Eng., **141**(8), p. 081007.
[38] Xu, Y., Wang, Z., Gong, S., and Chen, Y., 2021, "Reusable Support for Additive Manufacturing," Addit. Manuf., **39**.
[39] Xu, Y., Qi, F., Mao, H., Li, S., Zhu, Y., Gong, J., Wang, L., Malmstadt, N., and Chen, Y., 2022, "In-Situ Transfer Vat Photopolymerization for Transparent Microfluidic Device Fabrication," Nat. Commun., **13**(1), pp. 1–11.
[40] Li, X., Yuan, Y., Liu, L., Leung, Y.-S., Chen, Y., Guo, Y., Chai, Y., and Chen, Y., 2020, "3D Printing of Hydroxyapatite/β-Tricalcium Phosphate Scaffold With Hierarchical Porous Structure for Bone Regeneration," Bio-Des. Manuf., **3**(1), pp. 15–29.